Earthquake nucleation in intact or healed rocks

Nicolas Brantut[1], Robert C. Viesca[2]

Abstract. Earthquakes are generated because faults lose strength with increasing slip and slip rate. Among the simplest representations of slip-dependent strength is the linear slip-weakening model, characterised by a linear drop to a residual friction. However, healed fault rocks often exhibit some slip strengthening before the onset of weakening. Here we investigate the effect of such a slip-hardening phase on the initial growth of a slip patch and on the nucleation of rupture instabilities. We assume a piecewise linear strength vs. slip constitutive relation. We compute stress and slip distributions for in-plane or anti-plane rupture configurations in response to an increasing, locally peaked (parabolic with curvature κ) stress profile. In contrast with the strictly linear slip-weakening case, our calculations show that the curvature of the loading profile and the level of background stress strongly influence the nucleation size. Even for small amounts of slip hardening, we find that the critical nucleation size scales with $1/\sqrt{\kappa}$ for $\kappa \to 0$, i.e., crack growth remains stable up to very large crack sizes for sufficiently smooth loading profiles. Likewise, when the background stress τ_b is very close to the initial strength τ_c, the critical crack size scales with $1/\sqrt{\tau_\mathrm{c} - \tau_\mathrm{b}}$. An eigenvalue analysis shows that the nucleation length increases as the proportion of the crack undergoing slip-hardening increases, irrespective of the details of the loading profile. Overall, our results indicate that earthquake nucleation sizes can significantly increase due to slip hardening (e.g., in healed fault rocks), especially when the background loading is smooth.

1. Introduction

Within the Earth's brittle crust, deformation is localised along narrow shear faults. Slip along faults can be slow and stable, but is very sudden and dynamic during earthquakes. Laboratory experiments [e.g., *Ohnaka and Shen*, 1999; *Ohnaka*, 2000] and theoretical analyses [e.g., *Campillo and Ionescu*, 1997; *Rubin and Ampuero*, 2005; *Ampuero and Rubin*, 2008] have shown that periods of stable slip occur over some area along the fault immediately prior to dynamic slip, showing the existence of a nucleation phase of earthquake rupture. Of critical practical importance are the physical dimensions of the nucleation zone, and how they depend on the constitutive friction law and the loading configuration. In this paper, we focus our attention to earthquake nucleation along faults which are initially healed and locked.

At the kilometre scale, faults can be viewed as interfaces across which displacement discontinuities accumulate. However, faults are not atomically sharp planes and have a finite thickness, which may range from a few millimetres for the ultracataclasite core [*Chester and Chester*, 1998; *Chester et al.*, 2005], up to several hundred metres for the damage zone surrounding the core [e.g. *Sibson*, 2003]. Hence, "slip" on a fault should in fact be viewed as an integrated strain across the fault core.

Under subsurface conditions (typically 1 to 4 km depth), fault cores generally consist of an incohesive, granular gouge; at greater depths within the seismogenic zone (down to 10 to 15 km), fault rocks tend to be cohesive and form cemented cataclasites and/or mylonites [e.g. *Sibson*, 1977]. Along seismic faults, crack damage, grain comminution and disaggregation are generated during earthquakes, due to the very large strains and strain rate involved in the fault core. During the interseismic phase, as well as during periods when the fault is not active, the circulation of chemically active fluids, such as water, induces cementation of the fault core, especially under mid-crustal conditions where the ambient temperature and pressures are relatively high (of the order of several hundred degrees Celsius and tens to a hundred of megapascals) [e.g. *Tenthorey and Cox*, 2002; *Faulkner et al.*, 2008; *Smith et al.*, 2013]. The cementation of fault rocks corresponds to microcrack healing and mineralisation of pore space and open cracks [e.g. *Smith et al.*, 2013]; cemented fault rocks are thus expected to have regained cohesion (in contrast with granular fault gouges), and should have qualitatively similar mechanical properties to intact rocks [e.g. *Griffith et al.*, 2012]. Indeed, rock deformation experiment show that precompacted and healed fractures or sliding surfaces regain strength with time, and that they exhibit a similar stress-strain behaviour to intact rocks, which includes elastic loading, inelastic hardening, peak stress and subsequent strength drop [e.g. *Karner et al.*, 1997; *Nakatani and Scholz*, 2004; *Tenthorey and Cox*, 2002, see Figure 1]. In cohesive brittle materials such as rocks, the initial stage of inelastic strain-hardening originates from the growth of a network of tensile microcracks that gradually become connected to form a continuous shear fracture, whereas the post-peak behaviour is generally understood as pure frictional sliding on the fracture [*Paterson and Wong*, 2005].

Hence, slip on a cemented fault requires re-fracturing of the fault core and the overall shear strength of the fault is expected to initially increase with increasing slip (i.e., integrated strain across the fault core) before reaching a peak, and then to decrease. The apparent frictional behaviour is thus slip-hardening and then slip-weakening.

The hardening which precedes the peak stress has often been neglected in friction studies, and only the remaining post-peak slip-weakening behaviour is generally accounted for in representations of a rate-independent fault shear strength [e.g. *Palmer and Rice*, 1973; *Uenishi and Rice*, 2003]. As shown by *Uenishi and Rice* [2003], a remarkable aspect of linear slip-weakening laws is that the earthquake nucleation size, i.e., the critical size of the slip patch beyond which slip becomes dynamic, is a sole function of the shear modulus of the rock and the linear weakening rate of the shear strength, and does not depend upon the loading configuration and shape.

The purpose of the present work is to study earthquake nucleation along healed faults, by investigating the effect of a nonnegligible hardening phase prior to peak stress (as exemplified in Figure

[1]Rock and Ice Physics Laboratory and Seismological Laboratory, Department of Earth Sciences, University College London, London, UK.
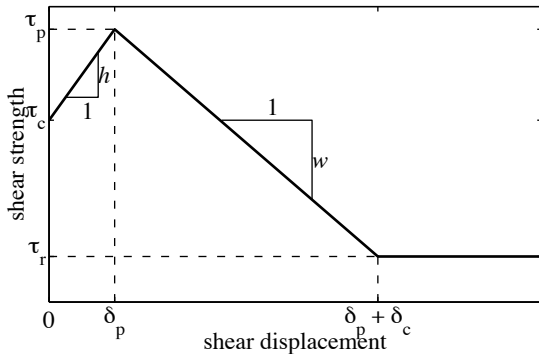[2]Civil and Environmental Engineering, Tufts University, Medford, MA, USA.
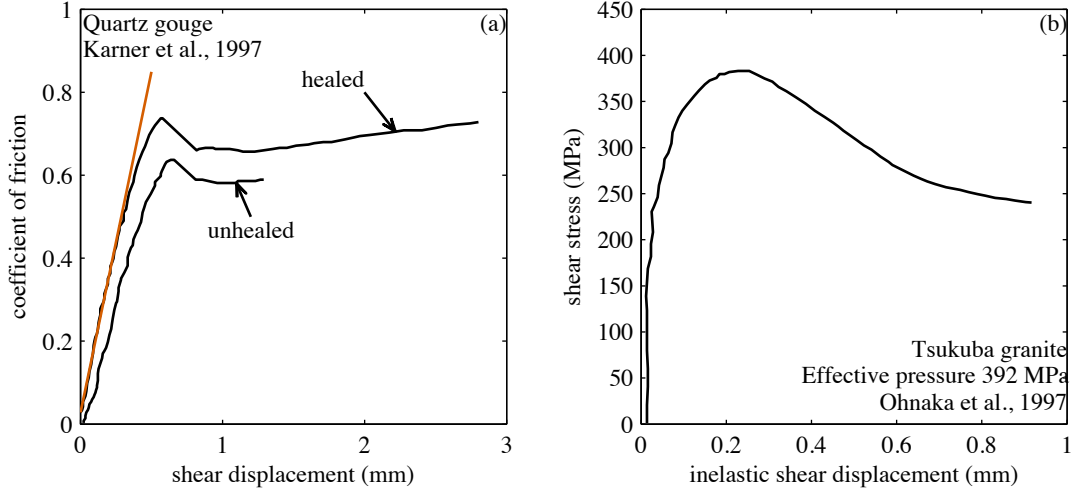
Figure 1. (a) Friction coefficient as a function of slip for quartz gouges deformed at 636°C. The healed gouge was held at 636°C for 10^4 s prior to deformation. Note that the peak stress is always preceded by some inelastic hardening. The red straight line corresponds to the elastic part of the slip displacement. Redrawn from *Karner et al.* [1997]. (b) Shear stress as a function of inelastic slip displacement for intact Tsukuba granite deformed at 392 MPa effective pressure. Redrawn from *Ohnaka et al.* [1997].

1) within a slip-dependent constitutive friction law. Our rheological model is qualitatively similar to that of *Stuart* [1979]; *Stuart and Mavko* [1979]; *Cao and Aki* [1984], who studied earthquake generation with a fault zone rheology that included an initial hardening phase; however, these authors did not study explicitly earthquake nucleation size, and a systematic comparison between results from pure slip-weakening and a rheology incorporating some slip-hardening remains to be performed. Within the framework of slip-hardening/weakening strength evolution, we investigate the effect of the loading profile on the critical crack size corresponding to the nucleation of a dynamic rupture instability.

2. Governing equations for quasistatic crack growth

2.1. Constitutive law for frictional slip

Experimental observations indicate that some slip-hardening often occurs prior to peak stress. In general the strength of the fault (i.e., the integrated strength of the rocks composing the fault core; see for instance *Ohnaka et al.* [1997]) should be described by the

Table 1. Examples of parameter values for initially intact Tsukuba granite; extracted from *Ohnaka et al.* [1997].

Effective pressure (MPa)	Temp. (°C)	Strain rate (/s)	h (MPa/mm)	w (MPa/mm)	δ_c/δ_p	w/h
471	456	$1.5\,10^{-4}$	335.8	22.6	8.1	0.07
392	25	$7\,10^{-6}$	964.5	169.8	3.7	0.18
470	450	10^{-5}	292.0	56.9	5.7	0.19
451	305	10^{-5}	486.8	98.3	2.8	0.20
180	25	10^{-5}	989.5	167.1	5.1	0.17
180	450	10^{-5}	416.6	34.1	7.1	0.08
180	300	10^{-5}	329.0	119.8	8.2	0.36
180	25	10^{-6}	1130.4	157.5	3.1	0.14
180	25	10^{-7}	195.7	99.3	3.9	0.51
253	355	10^{-6}	470.0	42.1	3.8	0.09

functional form that best reflects the deformation processes leading to the observed slip-hardening and the subsequent slip-weakening. Here we want to (1) minimise the number of parameters required to describe the strength evolution, and (2) use a functional form that can easily be related to the widely used linear slip-weakening law. Hence we adopt a phenomenological piecewise linear strength vs. slip relation:

$$\tau(\delta) = \begin{cases} \tau_c + h\delta & \text{for } 0 \leq \delta < \delta_p, \\ \tau_p - w(\delta - \delta_p) & \text{for } \delta_p \leq \delta < \delta_p + \delta_c, \\ \tau_r & \text{for } \delta_p + \delta_c \leq \delta. \end{cases} \quad (1)$$

Where $\tau(\delta)$ is the slip-dependent shear strength, τ_p is the peak stress, τ_c is the stress at the onset of slip (named after the classic notation C' defined by *Brace et al.* [1966] for the onset of inelastic strain), τ_r is the residual strength, δ_c is the critical slip weakening distance, and δ_p is the critical slip strengthening distance (i.e., the slip at peak stress). The hardening (h) and weakening (w) slopes are:

$$h = (\tau_p - \tau_c)/\delta_p, \text{ and } w = (\tau_p - \tau_r)/\delta_c. \quad (2)$$

The constitutive law is plotted in Figure 2. It reproduces the essential features observed experimentally (hardening followed by weakening), while minimising the number of additional parameters. In addition, after the peak strength is reached, the weakening is linear (with residual), and we retrieve the conventionally used slip-weakening law for further increases in slip.

Figure 2. Constitutive relation for shear strength as a function of slip. Slip starts at τ_c, followed by linear hardening up to τ_p, achieved at the critical slip distance δ_p, and then the behaviour is linear slip weakening down to a residual strength τ_r, associated with a weakening distance δ_c.

A set of representative parameter values for the model can be determined from experimental data obtained on intact rocks. Experimental data from *Ohnaka et al.* [1997] for the fracture of intact granite under a range of physical conditions are summarised in Table 1. We calculated representative values for the hardening rate h and the weakening rate w from the data provided by *Ohnaka et al.* [1997, (their Table 1)], by approximating the hardening and weakening phases by linear variations from the onset of slip to the peak and from the peak to residual strength, respectively. This procedure yields values of the order of 0.1 for the slope ratio w/h. The slip weakening distance is generally of the order of a few millimetres, and the ratio of weakening to hardening distances δ_c/δ_p ranges from 3 to 8.

2.2. Geometry and static equilibrium

We consider a finite crack embedded in an isotropic elastic medium, which is progressively loaded as a function of time. The shear stress τ at a position x along the crack line is given by [*Bilby and Eshelby*, 1968]

$$\tau(x,t) = \tau_b + q(x,t) + \frac{\mu^*}{2\pi}\int_{a_-}^{a_+}\frac{\partial\delta/\partial\xi}{\xi-x}d\xi, \quad (3)$$

where a_- and a_+ are the left and right positions of the crack tips, respectively, τ_b is a uniform background stress, $q(x,t)$ is an arbitrary loading profile superimposed to τ_b, μ^* is equal to the shear modulus μ of the surrounding medium in mode III, and $\mu^* = \mu/(1-\nu)$ (ν being Poisson's ratio) in modes I and II, and $\delta(x)$ is the slip along the crack. Equation 3 corresponds to the stress distribution along a static crack at equilibrium.
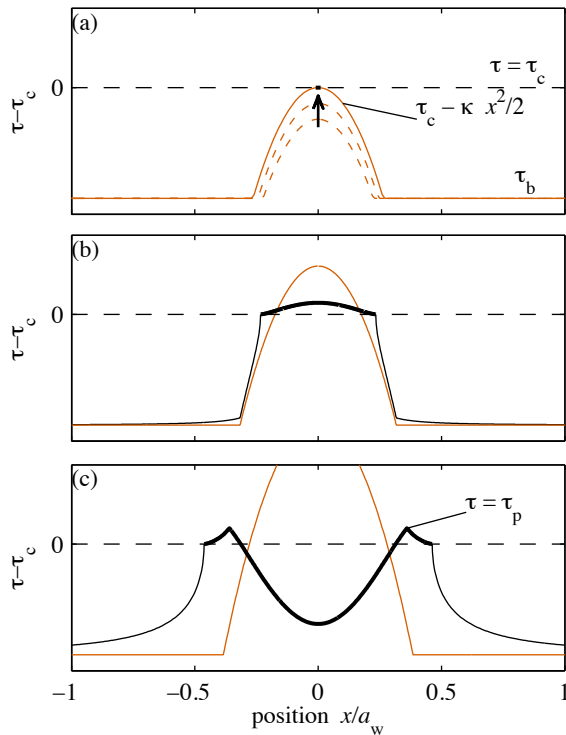
Figure 3. (a) Initial stress state (at $t = 0$) as a function of position x. Dotted red lines indicate previous instant ($t < 0$). At $t = 0$, the point $x = 0$ is just about to slip, as the imposed stress has just reached the strength τ_c. (b) The thick black line indicates the slipping region, which is here in the hardening phase. (c) The central part of of the crack is now in the weakening phase, while near the tips the fault remains hardening.

Throughout this paper we use the following particular loading shape [similar to that used by *Uenishi and Rice*, 2003]:

$$q(x,t) = \max\{0, Rt - \kappa x^2/2\}, \quad (4)$$

which provides a locally peaked profile parameterised by κ, which is a measure of the broadness of the loading, and a loading rate R (t is the time). The loading profile is a rising parabola, symmetric with respect to $x = 0$. Because of this symmetry, the crack will also be symmetric with respect to $x = 0$, and we have $a_+ = -a_- \equiv a$. The use of a locally peaked loading profile such as (4) allows us to investigate the effect of stress heterogeneities on earthquake nucleation with a simple parameterisation.

For convenience, we choose a reference time frame such that at $t = 0$, the imposed stress has just reached the fault strength at the point $x = 0$, i.e., $\tau_b + q(0,0) = \tau_c$ at $t = 0$. This initial stress state is shown graphically in Figure 3a.

Hence we can rewrite the equation for elastic equilibrium as

$$\tau(x) - \tau_c = \max\{\tau_b - \tau_c, Rt - \kappa x^2/2\} + \frac{\mu^*}{2\pi}\int_{-a}^{a}\frac{\partial\delta/\partial\xi}{\xi-x}d\xi. \quad (5)$$

3. Nucleation for parabolic loading

The procedure used to determine dynamic nucleation crack sizes follows that of *Uenishi and Rice* [2003]. The shear load is progressively increased (t increases), and for each step in t we calculate the slip distribution along the crack, and the crack size a. The calculation procedure is given in Appendix A. Initially, as t increases, the crack size increases as well: this corresponds to a stable situation, since new equilibrium configuration can be determined at each step (see Figure 3b,c). However, we expect to reach values of t and a above which any load increment produces an unbounded crack growth: this is where dynamic crack growth occurs.

In the case of strictly linear slip-weakening before residual friction is engaged, *Dascalu et al.* [2000]; *Uenishi and Rice* [2003] have demonstrated that the critical crack size at nucleation a_c is

$$a_c = a_c^{sw} \approx 0.579 a_w, \quad (6)$$

where $a_w = \mu^*/w$. Remarkably, a_c^{sw} does not depend upon the loading profile. Here we investigate how the introduction of a linear hardening regime preceding the linear slip weakening phase modifies the value of a_c and its dependence upon the shape of the loading profile.
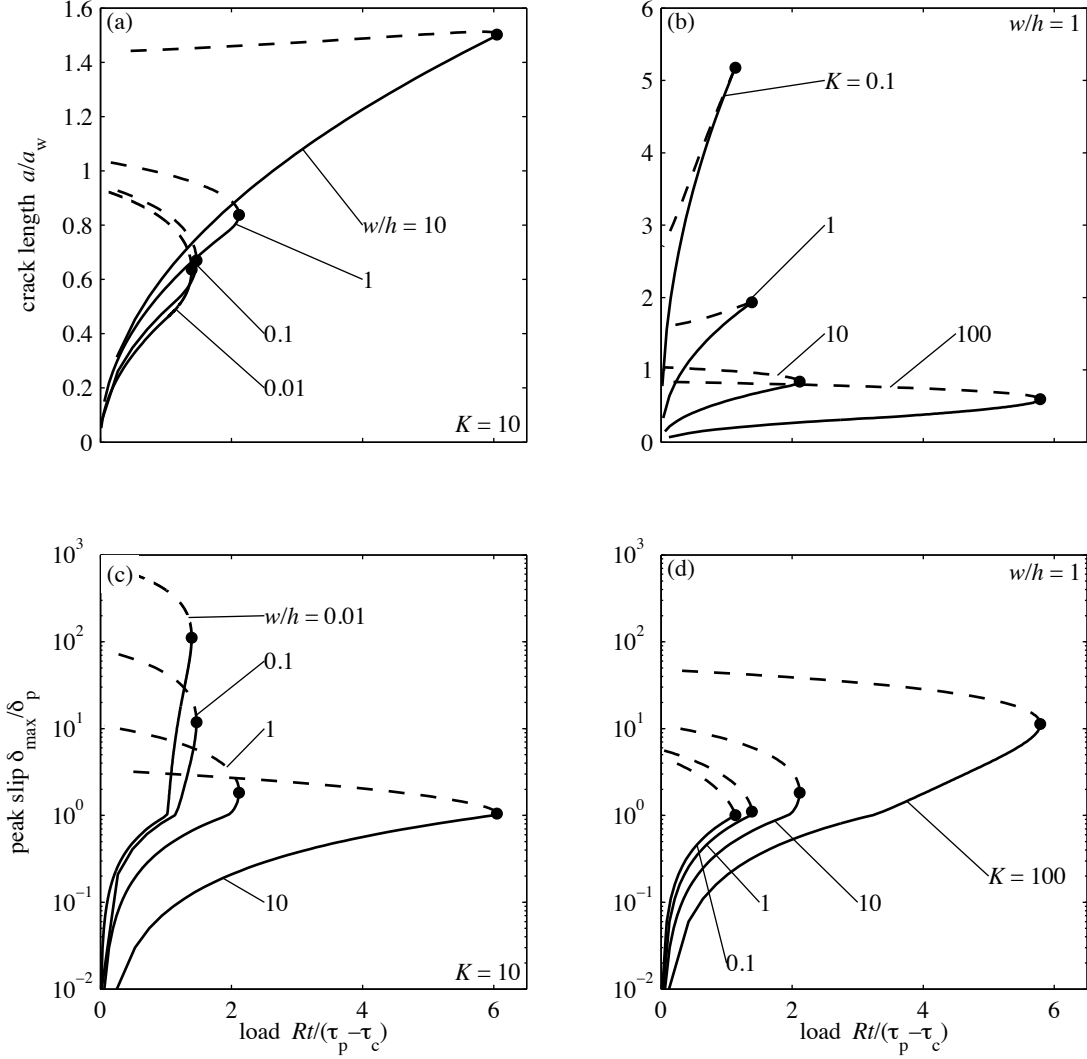
3.1. Small slip solutions, $\delta < \delta_p + \delta_c$

We first focus on the situations where nucleation occurs before a fully developed cohesive zone is established, i.e., for $\delta_{max} \leq \delta_p + \delta_c$. In such cases, the residual stress is not reached at any point during the quasistatic fault growth, and hence it does not influence the nucleation process. If we normalise slip by the hardening slip distance δ_p, and stress by $(\tau_p - \tau_c)$, the constitutive law becomes

$$(\tau - \tau_c)/(\tau_p - \tau_c) = \begin{cases} \delta/\delta_p & \text{if } \delta/\delta_p < 1, \\ 1 - (w/h)(\delta/\delta_p - 1) & \text{else,} \end{cases} \quad (7)$$

where we note that the only independent parameter is now the slope ratio w/h. The elastostatic equilibrium equation (5) can be rewritten in terms of the normalised slip δ/δ_p, stress $(\tau - \tau_c)/(\tau_p - \tau_c)$ and distance x/a as

$$\frac{\tau(x/a) - \tau_c}{\tau_p - \tau_c} = \max\left\{\frac{\tau_b - \tau_c}{\tau_p - \tau_c}, \frac{Rt}{\tau_p - \tau_c} - \frac{a^2\kappa(x/a)^2}{2(\tau_p - \tau_c)}\right\}$$
$$+ \frac{a_h/a}{2\pi}\int_{-1}^{1}\frac{\partial(\delta/\delta_p)/\partial\xi}{\xi-(x/a)}d\xi, \quad (8)$$

Figure 4. Equilibrium crack size a/a_w and peak slip δ_{max}/δ_p as a function of load $Rt/(\tau_p - \tau_c)$ for various weakening to hardening ratios ($w/h = 0.01$ to 10, panels (a) and (c)) and various curvatures of loading profile ($K = 0.1$ to 100, panels (b) and (d)). The critical nucleation size a_c/a_w, achieved when there is a vertical tangent to the crack size vs. load curves, is marked by a filled circle.

where

$$a_h = \frac{\mu^*}{h} = (w/h)a_w \qquad (9)$$

is an alternative characteristic crack length. We define a normalised curvature as

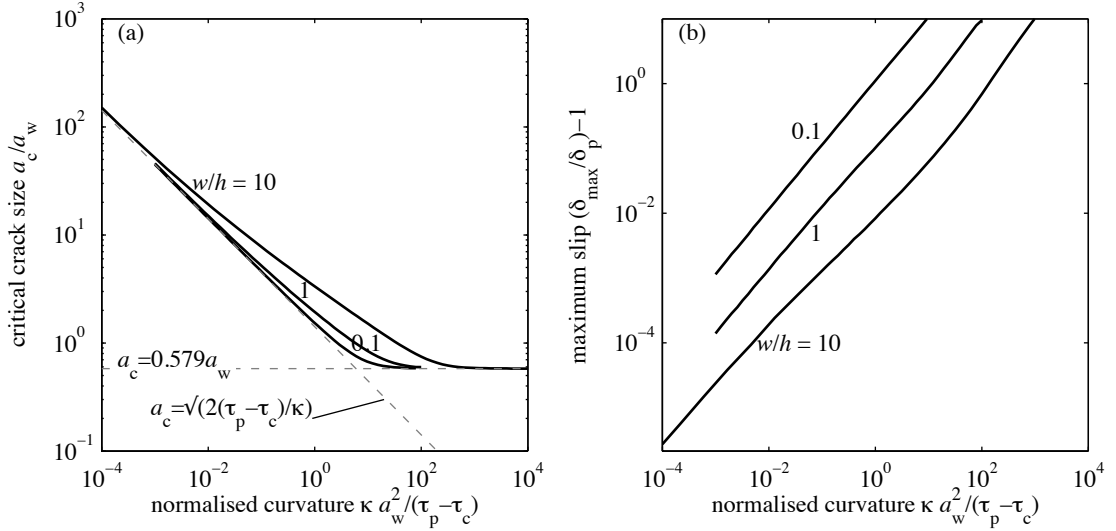$$K = \frac{\kappa a_w^2}{\tau_p - \tau_c}. \qquad (10)$$

We first investigate the cases for which the background stress is low enough so that $(\tau_b - \tau_c)/(\tau_p - \tau_c)$ is always below the imposed parabolic loading profile (i.e., the background stress). Figure 4 shows the solutions for load $Rt/(\tau_p - \tau_c)$ and crack size a/a_w with increasing maximum slip δ_{max} at the crack centre for various slope ratios w/h and curvatures K. In all cases, there is a peak load (marked by a filled circle) above which no static solution exists. The corresponding crack size is the critical nucleation size a_c.

Keeping the curvature constant ($K = 10$), we observe (Figure 4(a)) that the nucleation size increases modestly with increasing values of w/h, from around $0.64a_w \approx 1.10a_c^{sw}$ at $w/h = 0.01$ up to $1.50a_w \approx 2.59a_c^{sw}$ at $w/h = 10$. Concomitantly, the maximum slip (at the crack center) at the nucleation point increases from $\delta_{max} \approx 1.05\delta_p$ up to $\delta_{max} \approx 111.4\delta_p$ (Figure 4(c)). Of course, the critical size is reached for $\delta_{max} > \delta_p$, since the centermost part

of the fault needs to be in the weakening regime for the crack to grow unstably. For $w/h = 10$, the value of the maximum slip ($\delta_{max} \approx 111.4\delta_p$) is much larger than the typical values beyond which the residual strength is engaged (recalling that δ_c/δ_p ranges from 3 to 9 for granite); the solution given here under the small slip assumption (i.e., residual strength is never reached) serves only illustrative purposes, and we refer the reader to Section 3.2 for a discussion of the effect of residual frictional strength.

Holding the weakening to hardening ratio constant ($w/h = 1$), we observe (Figure 4(b)) that the nucleation size increases with decreasing curvature. For a very large curvature ($K = 100$), i.e., for a very peaked loading profile, the critical crack size is $a_c \approx 0.59a_w \approx 1.03a_c^{sw}$, but reaches $a_c \approx 5.17a_w \approx 8.93a_c^{sw}$ for a broad loading profile ($K = 0.1$). The corresponding maximum slip (plotted in Figure 4(d)) is correspondingly very large for peaked loading profiles ($\delta_{max} \approx 11.31\delta_p$ for $K = 100$) and decreases with decreasing curvature (down to $\delta_{max} \approx 1.01/\delta_p$ for $K = 0.1$).

A preliminary observation from Figure 4 is that both the constitutive parameter w/h and the shape of the loading profile (through its curvature K) influence the critical crack size. In particular, increasing the value of w/h by one order of magnitude tends to induce a moderate increase in a_c, while decreasing values of K tends to induce much larger changes in the nucleation size. In order to

Figure 5. Crack size (a) and maximum slip (b) at the nucleation point as a function of the curvature of the loading profile $K = \kappa a_\mathrm{w}^2/(\tau_\mathrm{p} - \tau_\mathrm{c})$.

understand the respective influence of the constitutive parameter w/h and curvature K in a quantitative manner, we computed a_c (as well as the maximum slip) for a wide range of K (from 10^{-4} up to 10^4) and for w/h ranging from 0.1 up to 10. The results are plotted in Figure 5. Figure 5(a) shows very clearly the increase in a_c (well above a_w) with decreasing curvature. Concurrently, Figure 5(b) indicates that the maximum slip (at the crack center) tends to the slip hardening distance.

The behaviour at small K can be explained as follows. The constitutive response is initially hardening, until the slip reaches the hardening distance δ_p. Thus, as long as the accumulated slip along the crack remains below δ_p, the crack will grow in a stable manner. If the loading profile has a very small curvature, we expect stable crack growth up to large crack sizes (as long as the maximum slip remains less than δ_p, i.e., before peak stress); then, unstable growth is expected when the center of the crack (where the maximum slip is achieved) starts weakening. This is illustrated in Figure 6, which shows the stress and slip profiles along the crack at the nucleation point for a case when $K = 10^{-3}$. The maximum slip is just above

the slip hardening distance, and only a very small portion of the crack (around 0.8%) has started weakening.

The scaling of a_c with K for $K \to 0$ can be determined as follows. When the crack size a grows in a stable manner well beyond the length scale a_h, i.e., $a_\mathrm{h}/a \ll 1$, which is allowed for small curvatures as long as $\delta_\mathrm{max} \leq \delta_\mathrm{p}$, then the integral term in (8) can be neglected. In that case, when the peak stress is reached at the crack center, we have $Rt/(\tau_\mathrm{p} - \tau_\mathrm{c}) \sim 1$, and the condition of no slip at $x = a$ yields
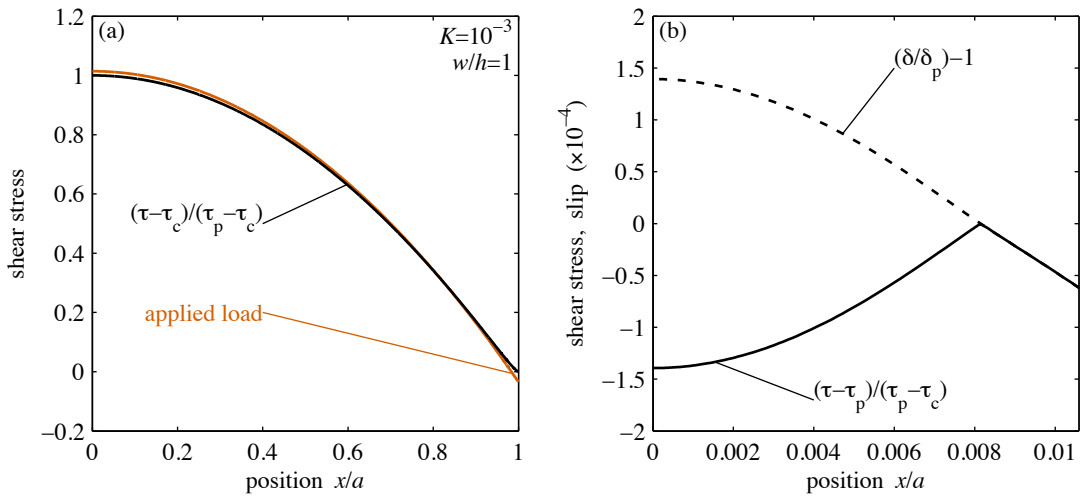
$$\frac{Rt}{\tau_\mathrm{p} - \tau_\mathrm{c}} - \frac{a^2 \kappa}{2(\tau_\mathrm{p} - \tau_\mathrm{c})} \sim 0. \tag{11}$$

If we then assume that nucleation occurs for $\delta_\mathrm{max} \sim \delta_\mathrm{p}$, we have the following asymptote for the critical crack size:

$$a_\mathrm{c} \sim \sqrt{\frac{2(\tau_\mathrm{p} - \tau_\mathrm{c})}{\kappa}}. \tag{12}$$

The scaling given in (12) is shown as a dotted line in Figure 5a.

Up to this point we have only looked at solutions for very low background stress $\tau_\mathrm{b} \ll \tau_\mathrm{c}$, and hence the solutions were not sensi-


Figure 6. Profiles of shear stress (solid black line), imposed load (solid red line) and slip (dotted black line) at the nucleation point for the case $K = 10^{-3}$ and $w/h = 1$. Panel (b) is a close up view near the crack centre, where the fault is weakening.

tive to τ_b. When τ_b becomes comparable to τ_c, a significant portion of the crack is under the influence of the background stress itself and not only of the superimposed parabolic load profile.

Figure 7 reports the critical crack size as a function of the fault "understress" $(\tau_c - \tau_b)/(\tau_p - \tau_c)$ for w/h ranging from 0.1 to 10. The critical crack size increases with decreasing understress (i.e., as the background stress becomes closer and closer to the stress at the onset of slip); simulation results show that a_c/a_w tends to scale with $1/\sqrt{(\tau_c - \tau_b)/(\tau_p - \tau_c)}$ when $(\tau_c - \tau_b)/(\tau_p - \tau_c) \to 0$.

An example of slip and stress profile at the nucleation point for a very low understress is given in Figure 8. The applied loading profile is peaked only at the center, and most of the crack is under the influence of the background stress. Unlike the case of small curvatures ($K \ll 1$), the slip at the crack center is significantly larger than the critical hardening distance δ_p. Despite the large crack size, the shear stress change and slip along the crack is very small far
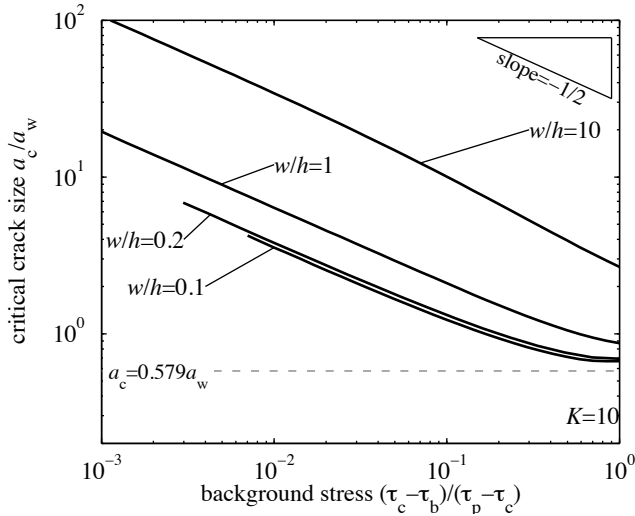
Figure 7. Critical crack size a_c/a_w as a function of background stress (or "understress") $(\tau_c - \tau_b)/(\tau_p - \tau_c)$, for normalised peak stresses ranging from 0 (grey curve) to 0.1, and normalised slip hardening distances of 0.02 and 0.1. For nonzero hardening, the critical crack size scales with the inverse square root of the background stress (see slopes in the top right corner).
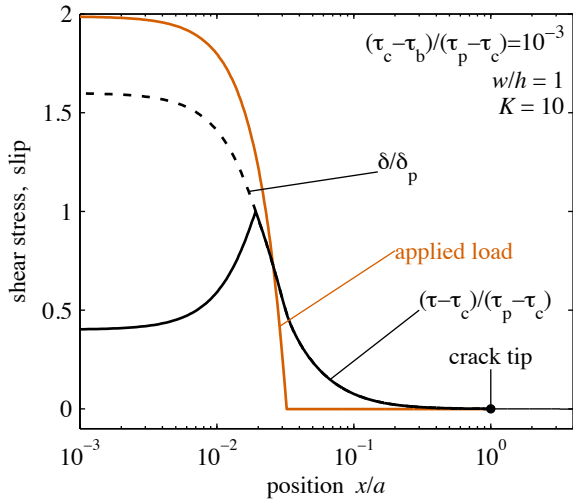
Figure 8. Shear stress, load and slip profile at nucleation ($a = a_c$) for a very small understress $(\tau_c - \tau_b)/(\tau_p - \tau_c) = 10^{-3}$. Note that a log scale is used for the x-axis.

from the crack center. In the example shown in Figure 8, δ/δ_p and $(\tau - \tau_c)/(\tau_p - \tau_c)$ are less than 10^{-2} for $x/a > 0.285$. Because of this very small slip and stress at the crack edges, the crack tip is barely identifiable when looking at the slip and stress profiles along the crack line.

### 3.2. Large slip solutions, $\delta > \delta_p + \delta_c$, and small scale yielding

When the slip along the crack reaches $\delta_p + \delta_c$, the shear strength becomes equal to the residual value τ_r. In all the situations described in the previous sections, the nucleation point occurs before the residual strength is reached. However, the residual strength affects the crack propagation beyond the small slip nucleation point, and can sometimes suppress the existence of a small slip nucleation point if it is reached early on during crack propagation: As slip accumulates along the crack and residual strength is engaged, we expect that new stable configurations can be reached, depending on the background stress level [*Viesca and Rice*, 2012; *Garagash and Germanovich*, 2012].

From a basic energetic consideration, we can first remark that if the background stress is lower than the residual strength ($\tau_b < \tau_r$), the crack is expected to be *ultimately* stable, i.e., there exists a crack size at which a quasistatic equilibrium solution is met. For background stresses larger than the residual strength, a range of scenarios is possible.

In order to explore the behaviour of the system at large slip, it is more natural to rescale stresses by the strength drop $(\tau_p - \tau_r)$ and slips by the slip weakening distance δ_c. For simplicity and consistency, we keep the same nondimensional parameters K and w/h for the description of the curvature and constitutive law, respectively. Figure 9 shows equilibrium solutions computed up to large slip $\delta_{max} > \delta_p + \delta_c$, for a range of background stresses. For illustrative purposes we set the slip weakening distance at ten times the slip hardening distance (an upper bound of the δ_c/δ_p values reported in Table 1). For $K = 10$ (panels a and b), nucleation occurs at small slip for $\delta_{max}/\delta_c = 0.183$. Here, the background stress is far enough from the stress at slip onset and it does not affect the critical crack size. The crack starts propagating dynamically immediately after the first nucleation point is reached, following the red arrow (increasing crack size and slip at constant load). When residual friction is engaged, we observe a strong effect of the background stress on crack propagation. For relatively low background stresses ($(\tau_c - \tau_b)/(\tau_p - \tau_r)$ from 0.75 to 0.9), a new stable configuration is met and dynamic crack propagation is expected to stop (if dynamic overshoot does not occur). If the imposed load is then further increased, another nucleation point is reached at large slip. An example of loading, slip and stress profiles along the crack at this point is shown in Figure 10, where we note the fully developed process zone near the crack tip. Conversely, for large enough background stresses ($(\tau_c - \tau_b)/(\tau_p - \tau_r) = 0.6$ or 0.7), no other stable branch is reached since the nucleation point at large slip occurs for a lower load than the initial, small slip nucleation point. In that case, the crack grows dynamically without stopping [*Viesca and Rice*, 2012; *Garagash and Germanovich*, 2012].

For a larger curvature of the loading profile ($K = 100$, Figure 9(c,d)), the situation is slightly different because the first nucleation point occurs for a maximum slip δ_{max} that is below but close to $\delta_p + \delta_c$. In those cases, the background stress has a small effect on the nucleation point at small slip. More importantly, for low enough background stresses (e.g., the cases $(\tau_c - \tau_b)/(\tau_p - \tau_r) = 0.7$ and 0.9), we note that the instability at small slip is almost suppressed because residual strength is engaged (and a stable branch appears) almost immediately beyond the first nucleation point. For large enough background stresses (e.g., $(\tau_c - \tau_b)/(\tau_p - \tau_r) = 0.3$), we do not expect any arrest of dynamic crack propagation since no other stable branch is reached beyond the first nucleation point.

Large slip solutions for crack size can be approximated by functions of the imposed load via a small scale yielding asymptotics approach, where we assume that the crack tip process zone is fully developed and small compared to the total crack size. The fracture

$$K = 10, \quad w/h = 1, \quad \delta_c/\delta_p = 10$$

$$K = 100, \quad w/h = 1, \quad \delta_c/\delta_p = 10$$
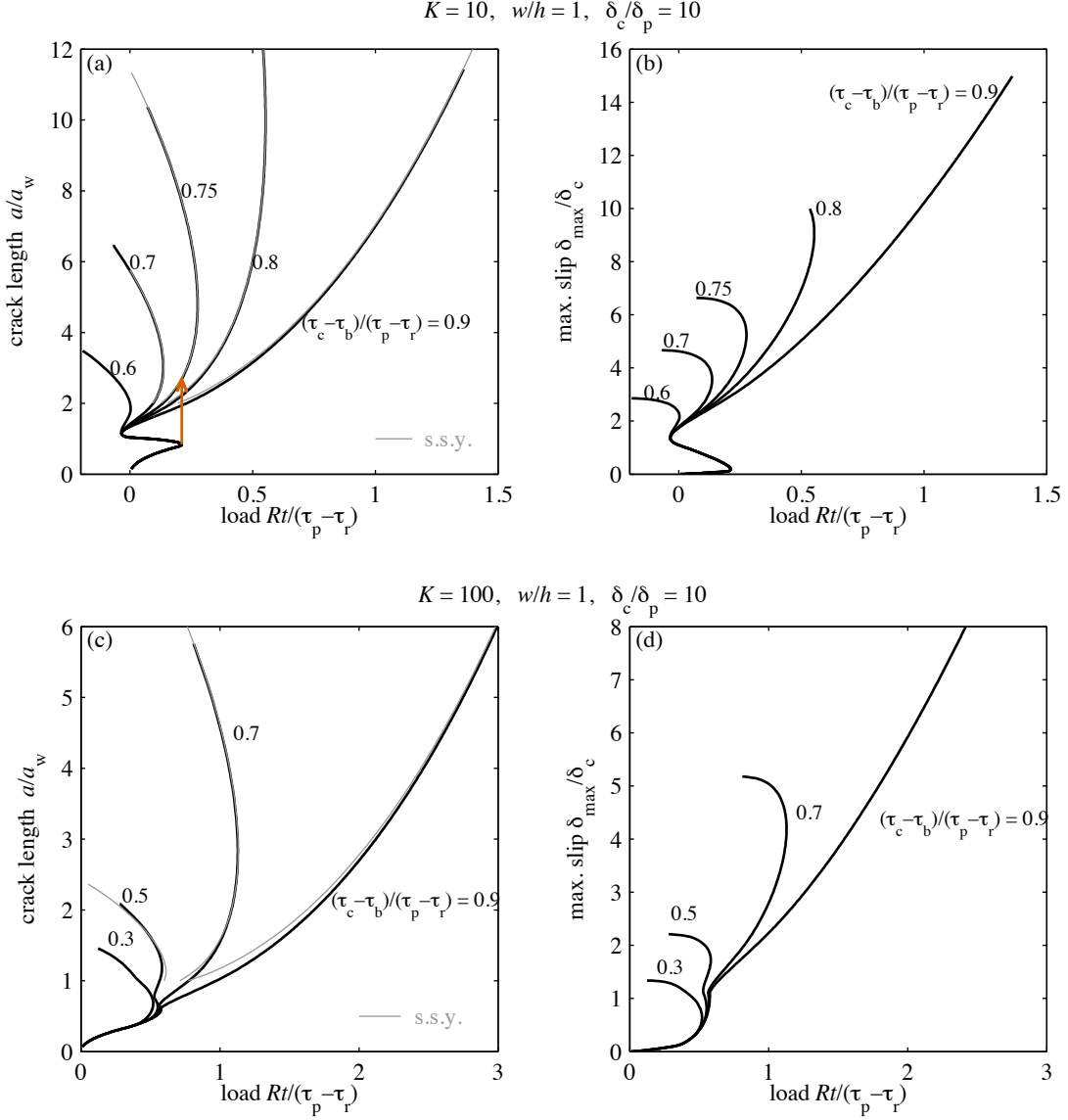
Figure 9. Crack size (a,c) and maximum slip (b,d) as a function of imposed load for background "understress" $(\tau_c - \tau_b)/(\tau_p - \tau_r)$ ranging from 0.3 to 0.9. Top panels (a,b): $K = 10$, bottom panels (c,d): $K = 100$. The small scale yielding approximation (s.s.y.) is plotted in grey. The red arrow indicates the potential jump in crack size from the small slip nucleation point to a new stable configuration at large slip.

energy for the slip hardening/weakening constitutive law is [*Rice*, 1968]:

$$G_c = \int_0^\infty (\tau(\delta) - \tau_r)d\delta = \frac{1}{2}(\tau_p - \tau_r)\delta_c + \left((\tau_p - \tau_r) - \frac{1}{2}(\tau_p - \tau_c) \right)\delta_p. \tag{13}$$

During crack propagation, this fracture energy has to be balanced by the energy release rate G at the crack tips. For a crack loaded by a stress equal to $\max\{\tau_b, Rt - \kappa x^2/2 + \tau_c\}$ on which the shear stress is equal to the residual strength τ_r, we can write the stress intensity factor k at the crack tips as [*Rice*, 1968]

$$k = \sqrt{\frac{a}{\pi}} \int_{-a}^{a} \frac{[\tau_b + \Delta\tau_b(x,t)] - \tau_r}{\sqrt{a^2 - x^2}} dx, \tag{14}$$

where the local increase in background stress is

$$\Delta\tau_b(x,t) = \max\{0, \tau_c - \tau_b + Rt - \kappa x^2/2\}. \tag{15}$$

A closed-form expression for k is given in Appendix B1. The energy release rate is then simply $G = k^2/(2\mu^*)$, and the small scale yielding propagation criterion is [*Rice*, 1968]

$$G_c = k^2/(2\mu^*). \tag{16}$$

Equation 16 is an approximation that presumes the details of the slip-weakening process zone occur over negligibly small distances relative to the crack length. However, we follow here the path given by *Garagash and Germanovich* [2012] who provide a better approximation by considering the finite size of process zone of an equilibrium slip-weakening crack in the semi-infinite limit [*Dempsey et al.*, 2010]. The method essentially consists in estimating the stress intensity factor in (16) using an effective crack size (instead of the total crack size a) accounting for the finite process zone size. Some details of the method are recalled in Appendix B2, but we refer the reader to the original works of *Dempsey et al.* [2010] and their adaptation by *Garagash and Germanovich* [2012] for further information. The resulting asymptotic behaviour is plot-

ted as thin grey lines in Figure 9, and shows a very good agreement with numerical simulations for large crack sizes.

4. General features of nucleation with piecewise linear hardening/weakening friction law

In the previous section, we have examined in detail the critical nucleation size and the associated slip profiles in the case of a locally parabolic loading. In two instances (small curvature and high background stress), we have determined that the nucleation size increases dramatically. Despite the differences in shape of the slip and loading profiles at the nucleation point, the common feature in both cases is that *the weakening region is concentrated at the crack centre* at the onset of instability. Here, we perform an eigenvalue analysis of the crack problem (3) and show that this feature of the linear hardening/weakening law is universal and does not depend on the specific choice of the loading shape.

Following the approach of *Uenishi and Rice* [2003], we differentiate equation (3) with respect to time and use the linear strength versus slip relation (1) to obtain

$$B(x)V(x,t) = R + \frac{\mu^*}{2\pi} \int_{-a}^{a} \frac{\partial V/\partial \xi}{\xi - x} d\xi, \quad (17)$$

where $V(x,t)$ is the slip rate along the crack, and

$$B(x) = \begin{cases} h & \text{for } x_p < |x| < a \\ -w & \text{for } |x| \leq x_p. \end{cases} \quad (18)$$

The points $\pm x_p$ satisfy $\delta(x) = \delta_p$. In other words, from the tips to x_p, the fault is slip strengthening, and from x_p to the crack centre, the fault is slip weakening. Note that the derivation of equation (17) relies on the nonsingularity condition for stress at the crack tips [see *Uenishi and Rice*, 2003, for more details about the derivation].

The slip rate V can be normalised by its root mean square V_{rms}. At the onset of nucleation V_{rms} becomes infinite, and the corresponding normalised slip rate v can be rewritten as

$$\frac{a}{a_w} b(x/a)v(x/a,t) = \frac{1}{2\pi} \int_{-1}^{1} \frac{\partial v/\partial \xi}{\xi - (x/a)} d\xi, \quad (19)$$

where $b(x/a) = B(x)/w$ (equal to -1 for $|x| \leq x_p$ and to h/w for $x_p < |x| < a$). Equation (19) is in the form of a generalised eigenvalue problem: we are looking for values of a/a_w such that nontrivial solution $v(x/a)$ of (19) exist. The smallest positive value of
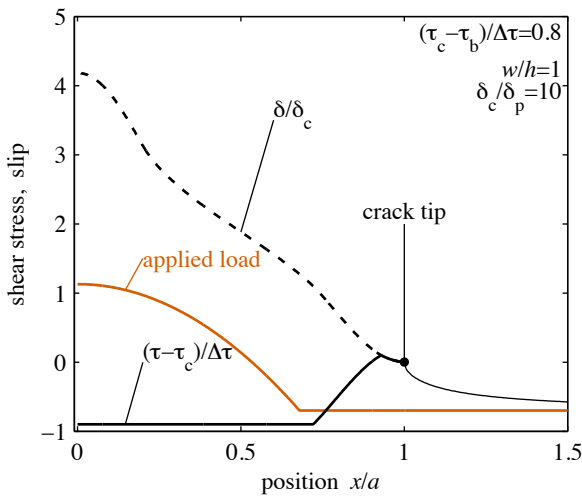
a/a_w gives us the nucleation length. By contrast with the problem analysed by *Uenishi and Rice* [2003] in the case of linear slip weakening, equation (19) contains additional parameters, h/w and x_p, which can be chosen arbitrarily.

The problem is solved following the methodology presented in Appendix C. The nucleation length given by the smallest positive eigenvalue of (19) is shown in Figure 11(a) as a function of x_p/a_c (the relative position of the transition point from slip hardening to slip weakening) for a range of values of w/h. For $x_p/a_c = 1$ we naturally retrieve the expected value of $a_c = 0.579a_w$, since the crack is entirely in the slip weakening regime. For decreasing values of x_p/a_c, the critical crack size increases. As x_p/a_c approaches 0, the critical crack size tends to infinity (i.e., nucleation will never occur, whatever the crack size, if the whole crack is in the hardening regime). For a given value of x_p/a_c, the critical crack size also increases with decreasing w/h. These results based on the eigenvalue analysis are consistent with the full numerical solutions presented previously: the critical crack size becomes large when a large proportion of the crack is in the hardening regime. Importantly, we show here that this behaviour does not depend upon the particular shape of the loading profile. The shape of the loading profile, and the value of the understress, are only driving the system towards a specific value of x_p. In other words, the loading profile influences the proportion of the crack that is undergoing hardening and weakening.

The transition point x_p gives the size of the weakened zone at nucleation. Figure 11(b) shows this size, normalised as x_p/a_w, as a function of the relative position of the transition point x_p/a_c. We

Figure 11. Critical crack size (a) and weakened zone size (b) as a function of the relative location of the peak strength along the crack.
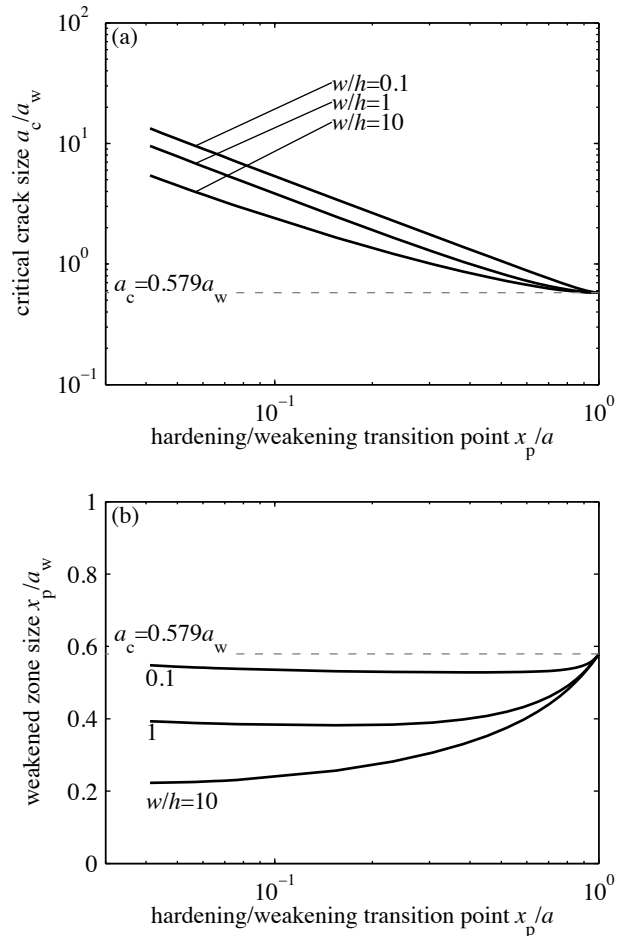
Figure 10. Shear stress, load and slip profile at nucleation for large slip. The imposed load curvature is $K = 10$. Other parameter values are reported in the Figure. The crack tip process zone is small compared to the total crack size.

observe that the weakened zone is systematically smaller than the critical crack size in the pure linear slip weakening case. Hence, approximating the fracture problem with slip hardening/weakening friction by simply neglecting the fraction of the crack experiencing slip hardening and only considering the slip weakening part of the crack would lead to a significant overestimate of the nucleation size.

5. Discussion

5.1. Choice and validity of the constitutive law

The slip-dependent constitutive law used here is merely a macroscopic description of the complex microscopic processes occurring during the brittle deformation of the fault core (e.g., asperity breakage, microcrack coalescence, sliding on grain boundaries...). Deformation across a fault occurs on a thin but finite-width shear zone, which might be healed due to cementation of the intergranular space [e.g. *Angevine et al.*, 1982]. The non-monotonic slip-dependent strength, including the slip hardening portion at the onset of slip, was chosen as a representative phenomenological description of the constitutive behaviour of intact rocks [e.g. *Paterson and Wong*, 2005], and, by extension, of the healed rocks forming the fault core (which can just be considered as "intact" regarding their mechanical properties). In fact, similar phenomenological laws have been used for the study of fault instability in the crust [*Stuart*, 1979; *Stuart and Mavko*, 1979; *Cao and Aki*, 1984; *Ohnaka and Yamashita*, 1989], and but the specificities arising from the slip-hardening behaviour before the peak stress had not seemed to be studied.

Slip-hardening followed by slip-weakening has been shown to arise naturally in micromechanical friction models based on slip across rough fault surfaces, as demonstrated by *Matsu'ura et al.* [1992]. In such a framework, the phenomenological parameters (stress at the onset of slip, peak stress, slip-hardening distance, etc) are related to physical parameters such as the asperity strength and statistical properties of the sliding surface topography (notably, the cut-off wavelength of surface roughness). A link between the constitutive friction parameters and the fault surface roughness implies that the constitutive law would itself be scale-dependent. Consequently, instabilities at small scales might occur, as observed for instance by acoustic emissions during the slip-hardening portion of the loading path during laboratory fiction experiments, while the overall fault remains stable at large scales.

We have made use here of a rate-independent constitutive law; however, we may have alternatively considered a law with both a rate and state dependence (where state may be represented via the history of slip rate –or slip– or some other internal variable), the most widely used friction laws of this class stemming from the work of *Dietrich* [1979]; *Ruina* [1983]. Here the strength at a point on the fault is determined by both a direct response to changes in slip velocity V and by the evolution of a state variable over a characteristic slip D_c. The relative importance of the two effects at any point on a slipping fault is determined by the ratio of two local time scales: the time scale associated with changes in velocity ($V/\partial V/\partial t$) and the time scale associated with state evolution (D_c/V) at a point on the fault. In regions where the former time scale is much shorter than the latter, slip-strengthening via the direct effect occurs, and when the converse is true (or if the time scales are comparable), then slip-weakening may be expected (provided the steady-state behavior is rate-weakening).

These laws apply for well developed slip surfaces in bare rock samples, but their validity for slip across thick gouge layers is not well understood, as the macroscopically observed constitutive parameters of the law vary with strain localisation, gouge thickness and particle size within the gouge layer [*Marone*, 1998]. Moreover, rate-and-state friction laws are designed to capture variations of frictional strength *around a well defined steady-state* sliding at constant slip rate: hence, these laws are not expected to provide a complete description of the early parts of slip across consolidated interfaces. Indeed, the slip-hardening/weakening behaviour does not seem to be a straightforward limiting case of any conventional rate-and-state friction law (unlike, for instance, the linear

slip-weakening model which corresponds to the "no-healing" limit of rate-and-state aging law [*Uenishi and Rice*, 2003; *Rubin and Ampuero*, 2005]).

5.2. Implications for earthquake nucleation in nature

Based on laboratory data obtained in granite [*Wong*, 1986], *Uenishi and Rice* [2003] provide numerical estimates of a_c^{sw} of the order of 0.5 to 0.9 m. As shown by our calculations, these values are lower bounds for the nucleation size of dynamic rupture. As observed in Section 3.1, the occurrence of even a moderate amount of slip-hardening prior to slip-weakening profoundly modifies the earthquake nucleation size, i.e., the size of the slipping region at the onset of dynamic rupture. In two different instances, for either broad loading profiles (small K) or background stresses close to initial strength (τ_b near τ_c), we observed that the nucleation size can become much larger than the one expected from pure slip-weakening friction.

For very broadly peaked loading profiles, we observed that the nucleation size scales with $\sqrt{2(\tau_p - \tau_c)/\kappa}$, that is to say, it scales with the size (radius of curvature) of the loaded patch. Hence, for very smoothly loaded faults, the earthquake nucleation size is dictated by the shape of the imposed tectonic stresses (modulated by the local pore pressures, when effective stresses are considered). By contrast, sharp loading profiles tend to induce localised slip and the hardening effects can be neglected. Natural fault surfaces are intrinsically rough, and the geometric constraints imposed by the fault roughness provide a source of inhomogeneity in the background stress. It is now well established that fault surface roughness is self-affine [e.g. *Candela et al.*, 2012], and hence there isn't a single dominant length scale that could be used to estimate a curvature for the background stress profile along a fault. Rather, a representative background stress profile would mimic the complex shape of the fault surface roughness. Such situations are beyond the scope of the present study, which was focused on a simple geometry in order to highlight the basic properties of the hardening/weakening constitutive law. It is clear that much work is needed to understand how complex fault stress patterns affect earthquake nucleation; Our simulations using a single length scale associated with loading constitutes a first essential step for the understanding of earthquake nucleation along such complex fault profiles.

The other situation where nucleation size becomes very large compared to the conventional slip-weakening critical length a_c^{sw} is
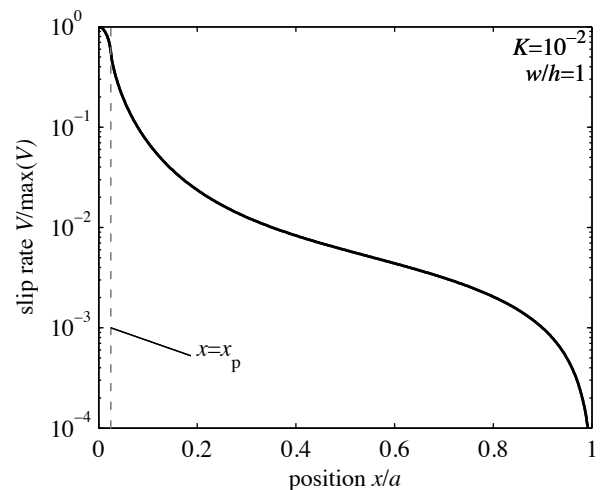
Figure 12. Profile of slip rate (normalised by its maximum value, located at the crack centre) at nucleation, computed numerically (as a finite difference) using the slip vs. load history. The parameter values chosen for this example are shown in the graph. The slip-weakening region ($x < x_p$) is where slip rate is within a small factor of the peak slip rate, and where inertial effects will first become important.

when the background stress τ_b becomes close to the initial strength τ_c. Remarkably, in those situations, the slip on the crack is essentially concentrated within a small portion near the crack centre: the hardening portion is very wide and could easily be mistaken for the stress concentration *ahead* of the crack tip (see Figure 8). The crack extends well beyond the locally applied peak load. These observations are of interest for the monitoring of fault deformation by remote sensing techniques or field measurements, and raise the issue of the identification of a crack tip using kinematic reconstructions. Indeed, in our simulations, the central weakening portion of the crack at the nucleation point can well be smaller than the critical nucleation size a_c^{sw} (as shown in Figure 11(b)) and yet the *whole* crack (including the wide hardening portions) becomes unstable.

Using the results of our quasi-static simulations, we can estimate the slip rate pattern along the crack immediately prior the onset of unstable slip; an example in given in Figure 12, where slip rate is computed as the finite difference between the slip patterns calculated for the last two load steps before the nucleation point. The slip rate is concentrated near the weakening region at the centre of the crack. In the moments immediately preceding dynamic rupture, the slip rate on the fault is accelerating everywhere, but relatively slowly in the area experiencing slip hardening as compared with the portion of the crack experiencing slip weakening. As observed previously (Figure 11), the portion of the crack experiencing slip weakening can be much smaller than the total crack size. Hence, such a phenomenon can help to rationalise experimental observations of rupture nucleation in rocks, in samples that may be smaller than the nucleation size a_c^{sw} [e.g. *Thompson et al.*, 2006]: a rupture may well appear to be quasistatic while the fault is slowly growing in the sample, but would start accelerating significantly within a small interior region experiencing slip weakening.

Our results suggest that a limited amount of quasistatic slip is likely to occur over large spatial scales prior to earthquake nucleation along initially locked, healed faults, such as intraplate continental faults with long earthquake recurrence times [e.g. *Scholz et al.*, 1986]. Immediately before earthquake nucleation, slip rate is accelerating nonuniformly along the fault, and the region experiencing the largest acceleration (here given approximately by x_p) can be localised within a very small patch relative to the dimension of the entire accelerating area. As a result, the inertial limitations on slip rate are first reached in the fastest accelerating patch, from which we expect the dynamic rupture to start propagating outward with concomitant emission of seismic waves. Additionally, the strong weakening mechanisms associated with these dynamic slip rates [*Di Toro et al.*, 2011] will also begin to operate here. One feature that sets our nucleation solutions apart from those using pure slip weakening friction is that the slip rates ahead of the fastest accelerating patch, although small, are also approaching rates at which strong weakening can occur. Furthermore, as seen for instance in Figures 6 and 8, the stress acting on the crack (beyond the onset of slip) is high, between τ_c and τ_p. Such high stresses, combined with the elevated slip rates at nucleation, are likely to enhance dynamic weakening mechanisms driven by heat production rate [see for example *Di Toro et al.*, 2011]. Taken together, these features could make the initial phases of dynamic rupture (initial rupture speed and starting phases) distinctly different between cases when $x_p/a_c \approx 1$ (i.e., the entire crack is slip weakening) and when $x_p/a_c \ll 1$ (i.e., the slip weakening zone is small).

6. Conclusions and perspectives

We have calculated earthquake nucleation sizes on faults obeying a non-monotonic, slip-hardening and weakening strength. The choice of the constitutive law was guided by laboratory observations of the fracture of intact and healed rocks. By contrast with linearly slip-weakening faults [*Uenishi and Rice*, 2003], the shape of the loading profile (here its curvature) has an influence on the nucleation size. If the loading profile is broad enough, the critical nucleation size can become much larger than the characteristic

slip-weakening nucleation size $a_c^{sw} \approx 0.579\mu^*\delta_c/(\tau_p - \tau_r)$, even for small amounts of slip hardening prior to the peak stress. In addition, for background stresses close enough to the initial strength of the fault, the crack size also becomes much larger than a_c^{sw}. Using an eigenvalue analysis, we have determined that a_c is expected to increase dramatically, independently form the specific form of the loading profile, when the proportion of the crack undergoing slip weakening is reduced.

In the situations when the nucleation size is very large, the slip immediately behind the crack tip is very small (see Figures 6 and 8), and the identification of a "crack tip" might be impossible in practice. The region of the crack where slip is large and where the instability is expected to initiate (the weakening portion) is smaller than a_c^{sw}.

One important implication of our results is that large scale, stable fault creep (albeit for limited amounts of cumulated slip) can occur on a fault prior to the nucleation of a dynamic rupture event. In contrast with nucleation simulations performed using rate-and-state friction laws [e.g. *Rubin and Ampuero*, 2005; *Ampuero and Rubin*, 2008], in our calculations the whole fault plane is not sliding. Hence we model here the initiation of slip along a fault that is initially perfectly locked, a situation arising in the context of reactivation of ancient (healed) faults due to changes in tectonic stresses or pore fluid pressures.

Despite the limitations of our assumed slip-dependent constitutive law, our results raise the importance of the complexity in the fault stress patterns in the nucleation of earthquakes. One natural origin for the complex background stress field along faults is their geometrical roughness. Further work combining complex fault stress profiles, pore fluid pressure variations, and more complete constitutive behaviour for intact or healed fault rocks is needed to better understand earthquake nucleation along ancient, dormant fault subjected to tectonic and/or anthropogenic loading (e.g., fluid or CO_2 injection).

Appendix A: Numerical methods

The numerical method employed to solve equation 8 simultaneously with equation 1 is essentially the same as the one described by *Viesca and Rice* [2012]. The idea is to use a Gauss-Chebyshev quadrature rule for a singular integral transform [*Erdogan and Gupta*, 1972] to calculate the shear stress at discrete collocation points using the values of the slip gradient at discrete nodes along the crack. Then the equality between the shear strength (given by the constitutive law) and the shear stress (given by the slip distribution) yields an equation for the slip distribution, which is solved by an iterative Newton-Raphson algorithm.

The nondimensional form of the equilibrium equation is

$$\tilde{\tau}(X) = T - \frac{K(\tilde{a}X)^2}{2} + \frac{1}{2\pi\tilde{a}}\int_{-1}^{1}\frac{\partial\tilde{\delta}}{\partial\xi}\frac{1}{\xi - X}d\xi, \qquad (A1)$$

where $\tilde{\tau} = (\tau - \tau_c)/\Delta\tau$, $\tilde{a} = a/a_w$ and $X = x/a$. For simplicity in the description of the method, we omitted the constant background stress in equation A1. Because stresses and slip are symmetric with respect to $X = 0$, it is convenient to rewrite (A1) for the space variable $Y = 2X - 1$:

$$\tilde{\tau}(Y) = T - \frac{K\tilde{a}^2(Y+1)^2}{8} + \frac{1}{\pi\tilde{a}}\int_{-1}^{1}\frac{\partial\tilde{\delta}}{\partial\xi}\left[\frac{1}{\xi - Y} + \frac{1}{\xi + Y + 2}\right]d\xi, \qquad (A2)$$

where Y ranges from -1 at the crack centre to 1 at the crack tip. The integral term is approximated by a Gauss-Chebyshev quadrature, which approximates

$$\int_{-1}^{1}\frac{f(\xi)}{\sqrt{1-\xi^2}}d\xi \approx \frac{\pi}{n}\sum_{j=1}^{n}f(\xi_j), \quad \text{for } \xi_j = \cos(\pi(2j-1)/(2n)). \qquad (A3)$$

To obtain an integrand of the form given in (A3), we define

$$\phi(\xi) = \frac{\partial\tilde{\delta}}{\partial\xi}\sqrt{1-\xi^2}, \qquad (A4)$$

and hence equation A1 can be written as

$$\tilde{\tau}(Y) = T - \frac{K\tilde{a}^2(Y+1)^2}{8} + \frac{1}{n\tilde{a}} \sum_{j=1}^{n} \phi(\xi_j) \left[\frac{1}{\xi_j - Y} + \frac{1}{\xi_j + Y + 2} \right],$$
(A5)

where the ξ_j ($j = 1, \dots, n$) are Chebyshev nodes

$$\xi_j = \cos\left(\pi \frac{2j-1}{2n} \right).$$
(A6)

The shear stress and slip are collocated at points $Y_i = \cos(\pi i/n)$ ($i = 1, \dots, n-1$). Equation A5 can then be rewritten in matrix form as

$$\tilde{\tau}[\tilde{\delta}_i] = T - \frac{K\tilde{a}^2(Y_i+1)^2}{8} + \frac{1}{\tilde{a}} E_{ij}\phi_j,$$
(A7)

where the dependency of $\tilde{\tau}$ on $\tilde{\delta}$ (arising from the constitutive slip-dependent friction law) was made explicit, and

$$\tilde{\delta}_i = \tilde{\delta}(Y_i),$$
(A8)

$$\phi_j = \phi(\xi_j), \quad \text{and}$$
(A9)

$$E_{ij} = \frac{1}{n} \left[\frac{1}{\xi_j - Y_i} + \frac{1}{\xi_j + Y_i + 2} \right].$$
(A10)

The discretised slip $\tilde{\delta}_i$ is expressed as a function of ϕ_j as

$$\tilde{\delta}_i = S_{ij}\phi_j.$$
(A11)

In order to compute the matrix S_{ij}, we can first remark that, according to the quadrature rule, ϕ_j can be expressed as a decomposition along the n first Chebyshev polynomials of the first kind:

$$\phi_j = \sum_{m=0}^{n-1} T_m(\xi_j)B_m = C_{jm}B_m,$$
(A12)

where $T_m(\cdot)$ denotes the m-th Chebyshev polynomial of the first kind, and B_m are the corresponding coefficients. Note that $C_{jm} = T_m(\xi_j) = \cos(m\pi(2j-1)/(2n))$. Following Equation A4, the slip at node i is then computed by direct integration of (A12), and is expressed as

$$\tilde{\delta}_i = D_{im}B_m,$$
(A13)

where

$$D_{im} = \begin{cases} -i\pi/n & \text{if } m = 0, \\ -(1/m)\sin(mi\pi/n) & \text{if } m \geq 1. \end{cases}$$
(A14)

The combination of (A12) and (A13) leads to the following expression for S_{ij}:

$$S_{ij} = D_{im}C_{jm}^{-1}.$$
(A15)

In order to determine C_{jm}^{-1}, which is the inverse of $T_m(\xi_j)$, we make use of the orthogonality of Chebyshev polynomials with respect to the weight $1/\sqrt{1-\xi^2}$:

$$\int_{-1}^{1} T_j(\xi)T_m(\xi) \frac{d\xi}{\sqrt{1-\xi^2}} = \begin{cases} \pi & \text{if } j = m = 0, \\ \pi/2 & \text{if } j = m \neq 0, \\ 0 & \text{else.} \end{cases}$$
(A16)

Using the quadrature rule (A3), the orthogonality condition (A16) implies that

$$\sum_{k=0}^{n-1} T_j(\xi_k)T_m(\xi_k) = \begin{cases} n/2 & \text{if } j = m = 0, \\ n & \text{if } j = m \neq 0, \\ 0 & \text{else,} \end{cases}$$
(A17)

and hence we obtain

$$C_{jm}^{-1} = \begin{cases} 1/n & \text{if } m = 0, \\ (2/n)\cos\big(m\pi(2j-1)/(2n)\big) & \text{if } m \geq 1. \end{cases}$$
(A18)

The relation A7 provides us with $n-1$ independent equations. There are n unknown values of ϕ_j, and the crack size $\tilde{a}$ is also an unknown. The relation between T and $\tilde{a}$ is non-monotonic, hence it is not convenient to impose T and attempt to find a. For practical purposes it is more efficient to let T be an additional unknown, and to impose the maximum slip, denoted $\tilde{\delta}_{\max}$, which always occurs at the crack centre (since the loading profile is symmetric). Hence we have $n+2$ unknown: $n-1$ values of ϕ_j, a and T. We need three additional constraints to close the system.

The first additional constraint comes from the requirement that there is no stress intensity factor at the crack tip (the crack is non singular). This implies that there is no slip gradient at the tip, which requires that $\phi(\xi = -1) = 0$ (note that this condition is necessary but, sensu stricto, not sufficient to impose zero slip gradient at the tip; however, the numerical computations using this weak condition always lead to the expected nonsingular solutions). There is no Chebyshev node at $\xi = 1$, but $\phi(\xi = 1)$ can be accessed via extrapolation of ϕ_j. The condition is then [*Viesca and Rice*, 2012]

$$0 = \phi(-1) \approx \frac{1}{n} \sum_{j=1}^{n} \frac{\sin(\pi(2n-1)(2j-1)/(4n))}{\sin(\pi(2j-1)/(4n))} \phi_{n+1-j}. \quad \text{(A19)}$$

A second additional constraint is that there must not be any slip gradient at the crack centre, because the loading profile is symmetric and the peak slip must occur at the centre. The condition is equivalent to imposing $\phi(-1) = 0$, and reads

$$0 = \phi(1) \approx \frac{1}{n} \sum_{j=1}^{n} \frac{\sin(\pi(2n-1)(2j-1)/(4n))}{\sin(\pi(2j-1)/(4n))} \phi_j. \quad \text{(A20)}$$

Finally, we impose the peak slip $\tilde{\delta}_{\max}$ at the centre of the crack ($Y = -1$), which yields the following constraint on ϕ_j:

$$\tilde{\delta}_{\max} = \tilde{\delta}(-1) = -\int_{-1}^{1} \frac{\partial \tilde{\delta}}{\partial \xi} d\xi \approx -\frac{\pi}{n} \sum_{j=1}^{n} \phi_j. \quad \text{(A21)}$$

Relations A7, A20, A19 and A21 form a nonlinear system of equations for the unknowns ϕ_j, $\tilde{a}$ and T. This system is solved using the Newton-Raphson algorithm.

Appendix B: Small scale yielding

Here we develop some of the formulas used in the calculation of the small scale yielding asymptotics.

B1. Stress intensity factor

We first give closed-form expressions for the stress intensity factor given in Equation 14. If we denote $x_0 = \sqrt{2(\tau_c - \tau_b + Rt)/\kappa}$ the point at which $\Delta\tau_b(x)$ first reaches 0, we have

$$k = (\tau_b - \tau_r)\sqrt{\pi a} + \Delta k(x_0),$$
(B1)

where

$$\Delta k(x_0) = \sqrt{\frac{a}{\pi}} \int_{-\min\{a,x_0\}}^{\min\{a,x_0\}} \frac{\tau_c - \tau_b + Rt - \kappa x^2/2}{\sqrt{a^2 - x^2}} dx.$$
(B2)

After some algebra, we find

$$\Delta k = \begin{cases} \sqrt{\frac{a}{\pi}} \arcsin\left(\frac{x_0}{a}\right) \left[2(\tau_c + Rt - \tau_b) - \kappa a^2/2 \right] \\ \qquad\qquad + \sqrt{\frac{a}{\pi}} \frac{\kappa}{2} x_0 \sqrt{a^2 - x_0^2} & \text{if } x_0 < a, \\ \sqrt{\pi a} \left[\tau_c + Rt - \tau_b - \kappa a^2/4 \right] & \text{else.} \end{cases}$$

B2. Improved asymptotics

We briefly recall here the method used to compute precise small scale yielding asymptotic solutions. We used the results from *Garagash and Germanovich* [2012], based on the works of *Dempsey et al.* [2010]. The method consists in replacing the crack size a by an effective crack size a_{eff} in the expression of the far field stress intensity factor $k(a)$ (in equation 14). For linear slip weakening with residual strength in the crack tip process zone, *Dempsey et al.* [2010] determined that the size of the process zone is

$$d \approx 0.466\lambda \qquad (B3)$$

for very large crack size (i.e. for $a - d \gg \lambda$), where $\lambda = (\pi/2)(k/(\tau_{\mathrm{p}} - \tau_{\mathrm{r}}))^2$ is a characteristic length scale. The ratio d/λ is expected to be slightly different from 0.466 in the case studied here because there is some slip hardening prior to the slip weakening behaviour. Considering cases where the slip strengthening distance is small compared to the slip weakening distance, we neglect the hardening region and use the above value of d/λ and find that the approximation is of reasonable quality (see Figure 9).

During crack propagation we have $k^2/(2\mu^*) = G_{\mathrm{c}}$, and hence λ can be estimated as $\lambda/a_{\mathrm{w}} = \pi G_{\mathrm{c}}/(\Delta\tau\delta_{\mathrm{c}})$. *Garagash and Germanovich* [2012] determined that an accurate estimate of the far-field stress intensity factor could be calculated when using

$$a_{\mathrm{eff}} = a - 0.466d \qquad (B4)$$

instead of a in the estimation of k, i.e., by reducing the total crack size by a fraction of the process zone size. Approximate solutions for crack size a/a_{w} as a function of the imposed load $Rt/\Delta\tau$ can then be calculated by using the crack propagation criterion (16) with the modified far-field $k(a_{\mathrm{eff}})$ (computed using (B1) and (B3)). Those solutions are plotted in Figure 9 in grey (labelled "s.s.y"). Despite the approximation made that the ratio d/λ would remain equal to 0.466, we observe that the asymptotic solution does a very good job for crack sizes a/a_{w} above 2. As a note of caution, however, we wish to note that this overall good quality of the modified small scale yielding asymptote might be deteriorated when choosing very large hardening distance and/or very large peak stress. In those cases, the ratio d/λ might be altered and a better correction could be desirable.

Appendix C: Eigenvalue problem

Using the nondimensional crack size $\tilde{a} = a/a_{\mathrm{w}}$ and coordinate $X = x/a$, equation (19) reads

$$\tilde{a}b(X)v(X) = \frac{1}{2\pi}\int_{-1}^{1}\frac{\partial v}{\partial \xi}\frac{d\xi}{\xi - X}. \qquad (C1)$$

We expect $\partial v(\xi)/\partial \xi$ to behave as $1/\sqrt{1-\xi^2}$ near the tips $\xi \pm 1$. This follows from the inversion of (C1), which gives [e.g., *Rice*, 1968]:

$$\frac{\partial v(X)}{\partial X} = \frac{2}{\pi}\frac{\tilde{a}}{\sqrt{1-X^2}}\int_{-1}^{1}\frac{\sqrt{1-\xi^2}}{\xi - X}b(\xi)v(\xi)d\xi, \qquad (C2)$$

where the integral is finite. Hence, we define

$$\psi(\xi) = \frac{\partial v}{\partial \xi}\sqrt{1-\xi^2}, \qquad (C3)$$

and use the Gauss-Chebyshev quadrature rule to obtain

$$\tilde{a}b(X)v(X) = \frac{1}{2n}\sum_{j=1}^{n}\frac{1}{\xi_j - X}\psi(\xi_j), \qquad (C4)$$

where $\xi_j = \cos(\pi(2j-1)/(2n))$. The slip rate v is collocated at points $X_i = cos(\pi i/n)$ ($i = 1,\ldots,n-1$). The discretised equation is rewritten in matrix form as

$$\tilde{a}A_{ij}\psi_j = K_{ij}\psi_j, \qquad (C5)$$

where $\psi_j = \psi(\xi_j)$, $K_{ij} = (1/2n)(1/(\xi_j - X_i))$, and

$$A_{ij} = b(X_i)S_{ij} \quad \text{(no sum on } i\text{)}. \qquad (C6)$$

The eigenvalues and eigenvectors are then obtained numerically using Matlab's function `eig`, setting $n = 801$.

References

Ampuero, J.-P., and A. M. Rubin, Earthquake nucleation on rate and state faults – Aging and slip laws, *J. Geophys. Res.*, *113*, B01302, doi: 10.1029/2007JB005082, 2008.

Angevine, C. L., D. L. Turcotte, and M. D. Furnish, Pressure solution lithification as a mechanism for the stick-slip behavior of faults, *Tectonics*, *1*(2), 151–160, 1982.

Bilby, B. A., and J. D. Eshelby, Dislocations and theory of fracture, in *Fracture, An advanced treatise*, vol. 1, edited by H. Liebowitz, pp. 99–182, Academic Press, San Diego, Calif., 1968.

Brace, W. F., B. W. Paulding Jr., and C. Scholz, Dilatancy in the fracture of crystalline rocks, *J. Geophys. Res.*, *71*(16), 3939–3953, 1966.

Campillo, M., and I. R. Ionescu, Initiation of antiplane shear instability under slip dependent friction, *J. Geophys. Res.*, *102*(B9), 20,363–20,371, 1997.

Candela, T., F. Renard, Y. Klinger, K. Mair, J. Schmittbuhl, and E. E. Brodsky, Roughness of fault surfaces over nine decades of length scales, *J. Geophys. Res.*, *117*, B08409, doi:10.1029/2011JB009041, 2012.

Cao, T., and K. Aki, Seismicity simulation with a mass-spring model and a displacement hardening-softening friction law, *Pure Appl. Geophys.*, *122*, 10–24, 1984.

Chester, F. M., and J. S. Chester, Ultracataclasite structure and friction processes of the Punchbowl fault, San Andreas system, California, *Tectonophysics*, *295*, 199–221, 1998.

Chester, J. S., F. M. Chester, and A. K. Kronenberg, Fracture surface energy of the Punchbowl fault, San Andreas system, *Nature*, *437*(1), 133–136, 2005.

Dascalu, C., I. R. Ionescu, and M. Campillo, Fault finiteness and initiation of dynamic shear instability, *Earth Planet. Sci. Lett.*, *177*, 163–176, 2000.

Dempsey, J. P., L. Tan, and S. Wang, An isolated cohesive crack in tension, *Continuum Mech. Thermodyn.*, *22*, 617–634, 2010.

Di Toro, G., R. Han, T. Hirose, N. De Paola, S. N. K. Mizoguchi, F. Ferri, M. Cocco, and T. Shimamoto, Fault lubrication during earthquakes, *Nature*, *471*, 494–498, 2011.

Dietrich, J. H., Modeling of rock friction: 1.experimental results and constitutive equations, *J. Geophys. Res.*, *84*, 2161–2168, 1979.

Erdogan, F., and G. D. Gupta, On the numerical solution of singular integral equations, *Q. Appl. Math.*, *29*, 525–534, 1972.

Faulkner, D. R., T. M. Mitchell, E. H. Rutter, and J. Cembrano, On the structure and mechanical properties of large strike-slip faults, in *The internal structure of fault zones: Implications for mechanical and fluid-flow properties*, *Special Publications*, vol. 299, edited by C. A. J. Wibberley, W. Kurz, J. Imber, R. E. Holdsworth, and C. Collettini, pp. 139–150, Geological Society, London, 2008.

Garagash, D. I., and L. N. Germanovich, Nucleation and arrest of dynamic slip on a pressurized fault, *J. Geophys. Res.*, *117*, B10310, doi: 10.1029/2012JB009209, 2012.

Griffith, W. A., T. M. Mitchell, J. Renner, and G. Di Toro, Coseismic damage and softening of fault rocks at seismogenic conditions, *Earth Planet. Sci. Lett.*, *353-354*, 219–230, 2012.

Karner, S. L., C. Marone, and B. Evans, Laboratory study of fault healing and lithification in simulated fault gouge under hydrothermal conditions, *Tectonophysics*, *277*, 41–55, 1997.

Marone, C., Laboratory-derived friction laws and their application to seismic faulting, *Annu. Rev. Earth Planet. Sci.*, *26*, 643–696, 1998.

Matsu'ura, M., . Kataoka, and B. Shibazaki, Slip-dependent friction law and nucleation processes in earthquake rupture, *Tectonophysics*, *211*(1), 135–148, 1992.

Nakatani, M., and C. H. Scholz, Frictional healing of quartz gouge under hydrothermal conditions: 1. Experimental evidence for solution transfer healing mechanism, *J. Geophys. Res.*, *109*, B07201, doi:10.1029/2001JB001522, 2004.

Ohnaka, M., A physical scaling relation between the size of an earthquake and its nucleation zone size, *Pure Appl. Geophys.*, *157*, 2259–2282, 2000.

Ohnaka, M., and L. Shen, Scaling of the shear rupture process from nucleation to dynamic propagation: Implications of geometry irregularity of the rupturing surfaces, *J. Geophys. Res.*, *104*(B1), 817–844, 1999.

Ohnaka, M., and T. Yamashita, A cohesive zone model for dynamic shear faulting based on experimentally inferred constitutive relation and strong motion source parameters, *J. Geophys. Res.*, *94*(B4), 4089–4104, 1989.

Ohnaka, M., H. Mochizuki, A. Odedra, F. Tagashira, and Y. Yamamoto, A constitutive law for the shear failure of rock under lithospheric conditions, *Tectonophysics*, *277*, 1–27, 1997.

Palmer, A. C., and J. R. Rice, The growth of slip surfaces in the progressive failure of over-consolidated clay, *Proc. Roy. Soc. Lond. A.*, *332*, 527–548, 1973.

Paterson, M. S., and T. F. Wong, *Experimental Rock Deformation – The Brittle Field*, 2nd ed., Springer-Verlag, Berlin Heidelberg, 2005.

Rice, J. R., Mathematical analysis in the mechanics of fracture, in *Fracture: An advanced treatise. Vol. 2: Mathematical fundamentals*, edited by H. Liebowitz, pp. 191–311, Academic Press, N.Y., 1968.

Rubin, A. M., and J.-P. Ampuero, Earthquake nucleation on (aging) rate and sate faults, *J. Geophys. Res.*, *110*, B11312, doi:10.1029/2005JB003686, 2005.

Ruina, A. L., Slip instability and state variable friction laws, *J. Geophys. Res.*, *88*, 10,359–10,370, 1983.

Scholz, C. H., C. A. Aviles, and S. G. Wesnousky, Scaling differences between large interplate and intraplate earthquakes, *Bull. Seism. Soc. Am.*, *76*(1), 65–70, 1986.

Sibson, R. H., Fault rocks and fault mechanisms, *J. Geol. Soc. Lond.*, *133*, 191–213, 1977.

Sibson, R. H., Thickness of the seismic slip zone, *Bull. Seism. Soc. Am.*, *93*, 1169–1178, doi:10.1785/0120020061, 2003.

Smith, S. A. F., A. Bistacchi, T. M. Mitchell, S. Mittempergher, and G. Di Toro, The structure of an exhumed intraplate seismogenic fault in crystalline basement, *Tectonophysics*, *599*, 29–44, 2013.

Stuart, W. D., Strain softening prior to two-dimensional strike slip earthquakes, *J. Geophys. Res.*, *84*(B3), 1063–1070, 1979.

Stuart, W. D., and G. M. Mavko, Earthquake instability on a strike-slip fault, *J. Geophys. Res.*, *84*(B5), 2153–2160, 1979.

Tenthorey, E., and S. F. Cox, Cohesive strengthening of fault zones during the interseismic period: An experimental study, *J. Geophys. Res.*, *111*, B09202, doi:10.1029/2005JB004122, 2002.

Thompson, B. D., R. P. Young, and D. A. Lockner, Fracture in Westerly granite under AE feedback and constant strain rate loading: Nucleation, quasi-static propagation, and the transition to unstable fracture propagation, *Pure Appl. Geophys.*, *163*, 995–1019, 2006.

Uenishi, K., and J. R. Rice, Universal nucleation length for slip-weakening rupture instability under nonuniform loading, *J. Geophys. Res.*, *108*(B1), 2042, doi:10.1029/2001JB001681, 2003.

Viesca, R. C., and J. R. Rice, Nucleation of slip-weakening rupture instability in landslides by localized increase of pore pressure, *J. Geophys. Res.*, *117*, B03104, doi:10.1029/2011JB008866, 2012.

Wong, T.-F., On the normal stress dependence of the shear fracture energy, in *Earthquake Source Mechanics*, *Geophys. Monogr. Ser.*, vol. 37, edited by S. Das, J. Boatwright, and C. H. Scholz, pp. 1–11, American Geophysical Union, Washington, DC, 1986.

N. Brantut, Rock and Ice Physics Laboratory, Department of Earth Science, University College London, Gower Street, London WC1E 6BT, UK. (n.brantut@ucl.ac.uk)

R. C. Viesca, Dept. of Civil and Environmental Engineering, Tufts University, 207A Anderson Hall, 200 College Avenue, Medford, MA 02155, USA. (robert.viesca@tufts.edu)